Supplement of Atmos. Chem. Phys., 26, 1229–1247, 2026
https://doi.org/10.5194/acp-26-1229-2026-supplement

Atmospheric Chemistry and Physics
Open Access

Supplement of

Methane fluxes from Arctic & boreal North America: comparisons between process-based estimates and atmospheric observations

Hanyu Liu et al.

Correspondence to: Hanyu Liu (hliu154@jhu.edu)

Details on the in situ tower sites

Tower Site	ID	Lat	Long	Elevation (masl)	Intake Height (magl)
Abbotsford	ABT	49.0°N	122.3°W	60	33
Bratt's Lake	BRA	50.2°N	104.7°W	595	35
Barrow Atmospheric Baseline Observatory	BRW	71.3°N	156.6°W	11	16
Behchoko	BCK	62.8°N	115.9°W	160	60
Cambridge Bay	CBY	69.1°N	105.1°W	35	12
Churchill	CHL	58.7°N	93.8°W	29	60
CARVE	CRV	65.0°N	147.6°W	611	32
Chapais	CPS	49.8°N	75.0°W	391	40
Egbert	EGB	44.2°N	79.8°W	251	25
Estevan Point	ESP	49.4°N	126.5°W	7	40
Esther	EST	51.7°N	110.2°W	707	50
East Trout Lake	ETL	54.4°N	104.9°W	493	105
Fort Nelson	FNE	58.8°N	122.6°W	361	15
Fraserdale	FSD	49.9°N	81.6°W	210	40
Hanlan's Point	HNP	43.6°N	79.4°W	87	10
Inuvik	INU	68.3°N	133.5°W	113	10
Park Falls	LEF	45.9°N	90.3°W	472	396
Lac La Biche	LLB	55.0°N	112.5°W	540	50
Toronto Atmospheric Observatory	TAO	43.7°N	79.4°W	100	174
Turkey Point	TPD	42.6°N	80.6°W	231	35
Sable Island	WSA	43.9°N	60.0°W	5	25

Table S1. Summary of 21 in-situ tall tower sites across Canada and the US, detailing their names, site codes, longitudes, latitudes, elevation (surface elevation in meters above sea level (masl)), and intake height (sample intake height in meters above ground level (magl)). Note that the abbreviation "CARVE" is short for "Carbon in Arctic Reservoirs Vulnerability Experiment."

Details on the GCP models

Model	Spatial Resolution (Rows $\times$ Columns)	References
$CH_4MOD_{wetland}$	360 x 720	Li et al., 2010
CLASSIC	53 x 128	Arora et al., 2018
DLEM	360 x 720	Tian et al., 2010
ELM-ECA	360 x 720	Zhu et al., 2019
ISAM	360 x 720	Shu et al., 2020
JSBACH	96 x 192	Kleinen et al., 2020
JULES	360 x 720	Clark et al., 2011
LPJ-GUESS	360 x 720	McGuire et al., 2012; Wania et al., 2010
LPJ-MPI	360 x 720	Kleinen et al., 2012
LPJ-wsl	360 x 720	Zhang et al., 2016
LPX-Bern	360 x 720	Spahni et al., 2011
ORCHIDEE	180 x 360	Ringeval et al., 2010
SDGVM	360 x 720	Singarayer et al., 2011
TEM-MDM	360 x 720	Liu et al., 2020
TRIPLEX-GHG	582 x 1440	Zhu et al., 2014
VISIT	360 x 720	Ito and Inatomi, 2012

Table S2. The 16 GCP global wetland flux models that we use in the study, including the number of global latitude and longitude grid cells in each model.

Details on the wetland to anthropogenic ratios at each in-situ tower site

Tower Site ID	Biome Type	Wetland to Anthropogenic Ratios
ABT	Temperate Forests	1.06
BRA	Temperate Grasslands	0.26
BRW	Tundra	0.85
BCK	**Boreal Forests/Taiga**	**8.79**
CBY	**Tundra**	**7.56**
CHL	**Boreal Forests/Taiga**	**14.00**
CRV	**Tundra**	**5.09**
CPS	**Boreal Forests/Taiga**	**2.51**
EGB	Temperate Forests	0.52
ESP	**Temperate Forests**	**3.57**
EST	Temperate Grasslands	0.34
ETL	**Boreal Forests/Taiga**	**1.31**
FNE	**Boreal Forests/Taiga**	**1.43**
FSD	**Boreal Forests/Taiga**	**3.93**
HNP	Temperate Forests	0.18
INU	**Boreal Forests/Taiga**	**9.17**
LEF	Temperate Forests	0.78
LLB	Temperate Grasslands	0.62
TAO	Temperate Forests	0.21
TPD	Temperate Forests	0.31
WSA	Temperate Forests	1.07

Table S3. The 21 in-situ tall tower sites with biome types and wetland to anthropogenic ratios. The ratios represent averages computed from prognostic and diagnostic model outputs, calculated as the modeled CAMS-derived CH_4 mixing ratios divided by the modeled mixing rations using the GCP models. In this study, we define sites with ratios greater than 1.3 as wetland-dominated. The sites in bold are the wetland-dominated sites used in our analysis, and we exclude other sites because they are more influenced by anthropogenic emissions.

Detailed groupings of prognostic GCP models based on their R^2 values

GCP Wetland Models	R^2 Values	Group
VISIT	0.5	High
CLASSIC	0.47	High
LPJ-wsl	0.46	High
LPJ-MPI	0.42	High
SDGVM	0.41	High
JSBACH	0.35	Average
LPX-Bern	0.34	Average
ORCHIDEE	0.32	Average
JULES	0.22	Low
ISAM	0.22	Low
ELM	0.21	Low

Table S4. Detailed groupings of prognostic GCP models based on their R^2 values. The table presents each GCP wetland model alongside its R^2 value and assigned group (High, Average, or Low) as determined by the performance criteria (High > 0.4; Average > 0.3; Low > 0.2).

Detailed groupings of diagnostic GCP models based on their R^2 values

GCP Wetland Models	R^2 Values	Group
LPJ-wsl	0.53	High
VISIT	0.5	High
LPJ-MPI	0.43	High
ISAM	0.42	High
CLASSIC	0.40	Average
JSBACH	0.39	Average
JULES	0.39	Average
SDGVM	0.37	Average
ORCHIDEE	0.34	Average
LPX-Bern	0.27	Low
ELM	0.22	Low

Table S5. Detailed groupings of diagnostic GCP models based on their R^2 values. The table presents each GCP wetland model alongside its R^2 value and assigned group (High, Average, or Low) as determined by the performance criteria (High > 0.4; Average > 0.3; Low > 0.2).

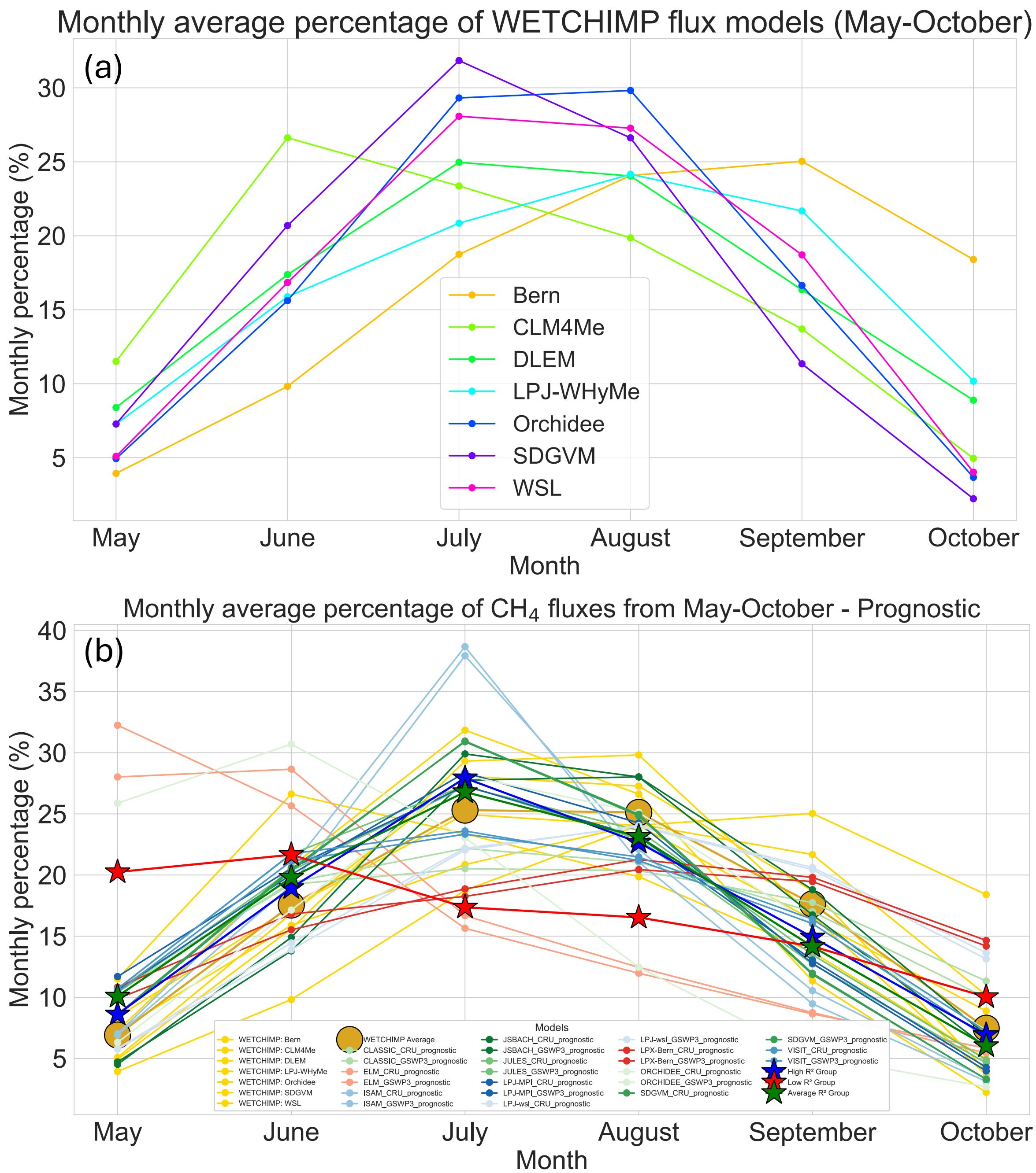

Figure S1. The seasonal cycles of the WETCHIMP models (a) and a comparison with the GCP models (b). In panel a, each colored line represents the percentage of fluxes that occurred in a specific model in that month compared to the total fluxes from that model for the months of May through October. Panel b displays the same quantity but also includes the GCP models. Each model is color-coded blue, green, or red lines to represent the GCP models that have the high, average, and low R^2 values, respectively, in the comparisons with atmospheric CH_4 observations. The yellow lines in this panel represent the WETCHIMP models.

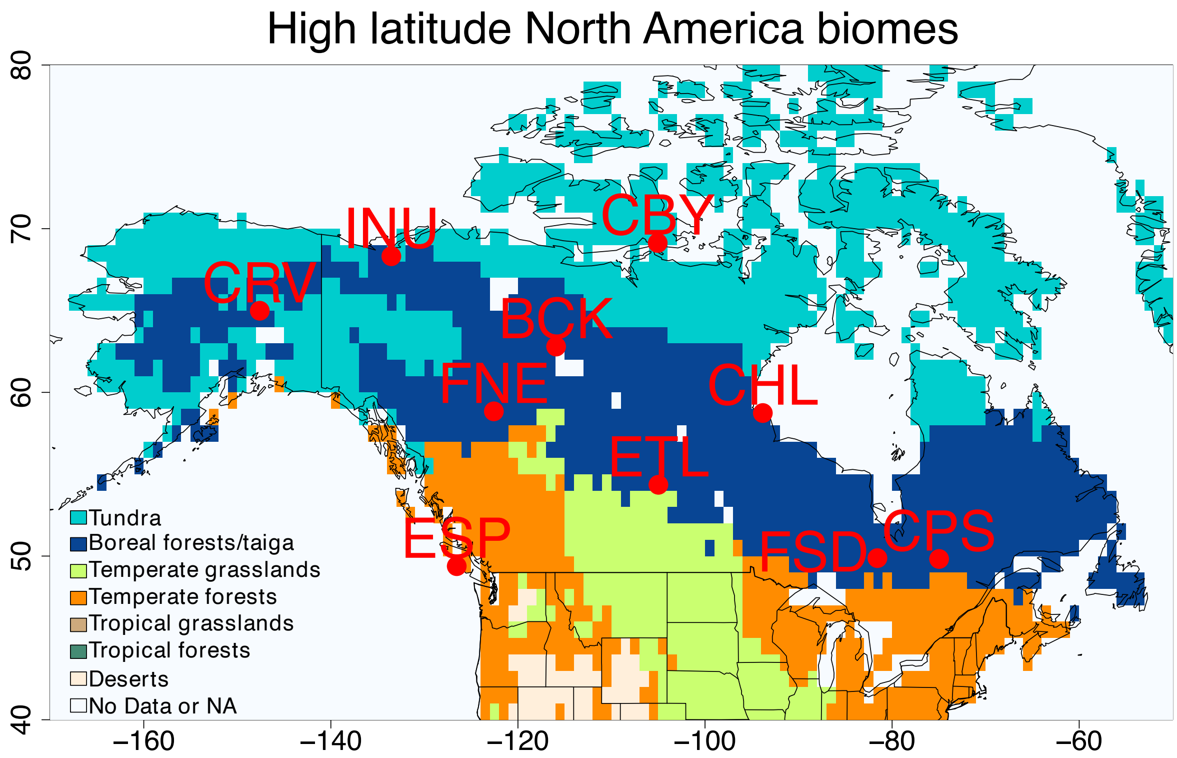

Figure S2. Biome map of high-latitude North America highlighting the three out of seven biome types examined in this study: Tundra and Boreal Forests/Taiga, and Temperate Forests. Red dots indicate wetland-dominated measurement sites, comprising a total of ten locations—nine across Canada and one in Alaska. Six sites (FNE, BCK, CHL, ETL, FSD, CPS) are located within the Boreal Forests/Taiga biome, three sites (CRV, INU, CBY) are within the Tundra biome, and one site (ESP) is located in the Temperate Forests biome. The biome map comes from the "Terrestrial Ecoregions of the World" product created by World Wildlife Fund (Olson et al., 2001).

Correlation coefficients

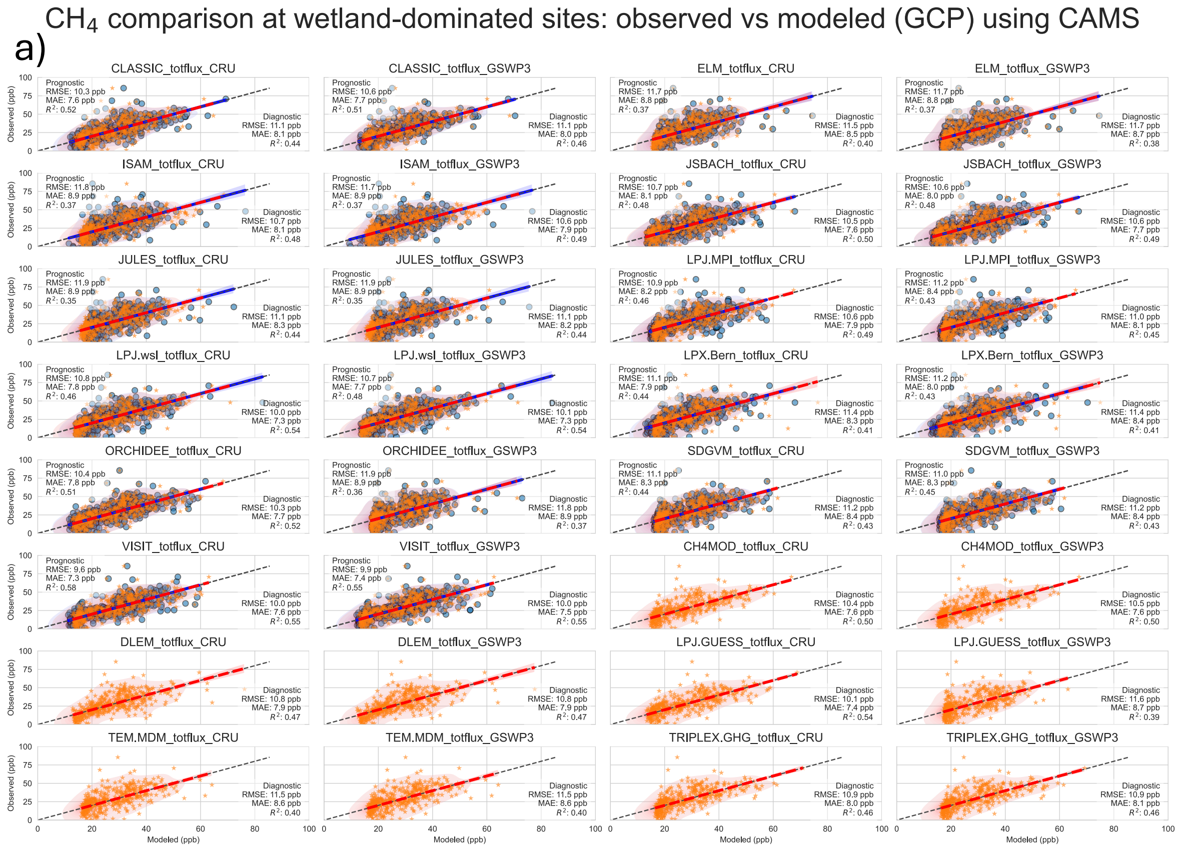

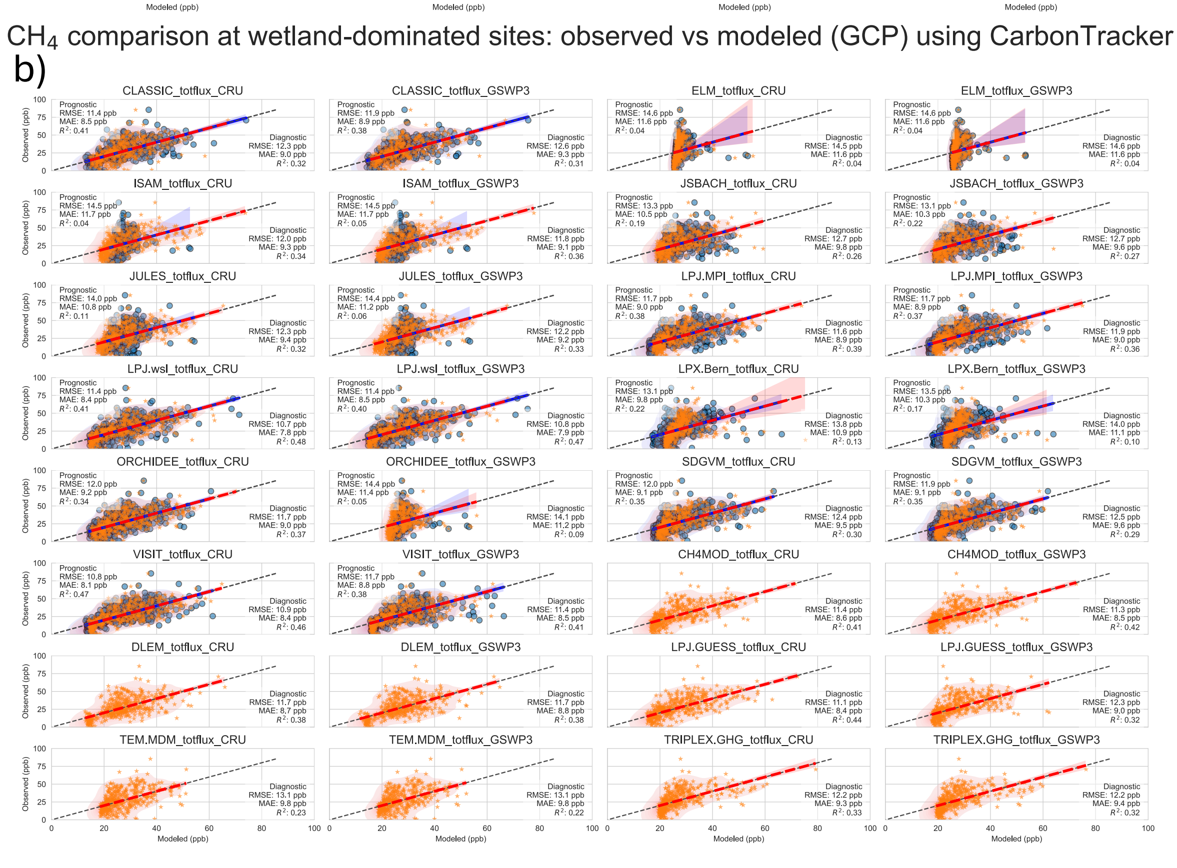

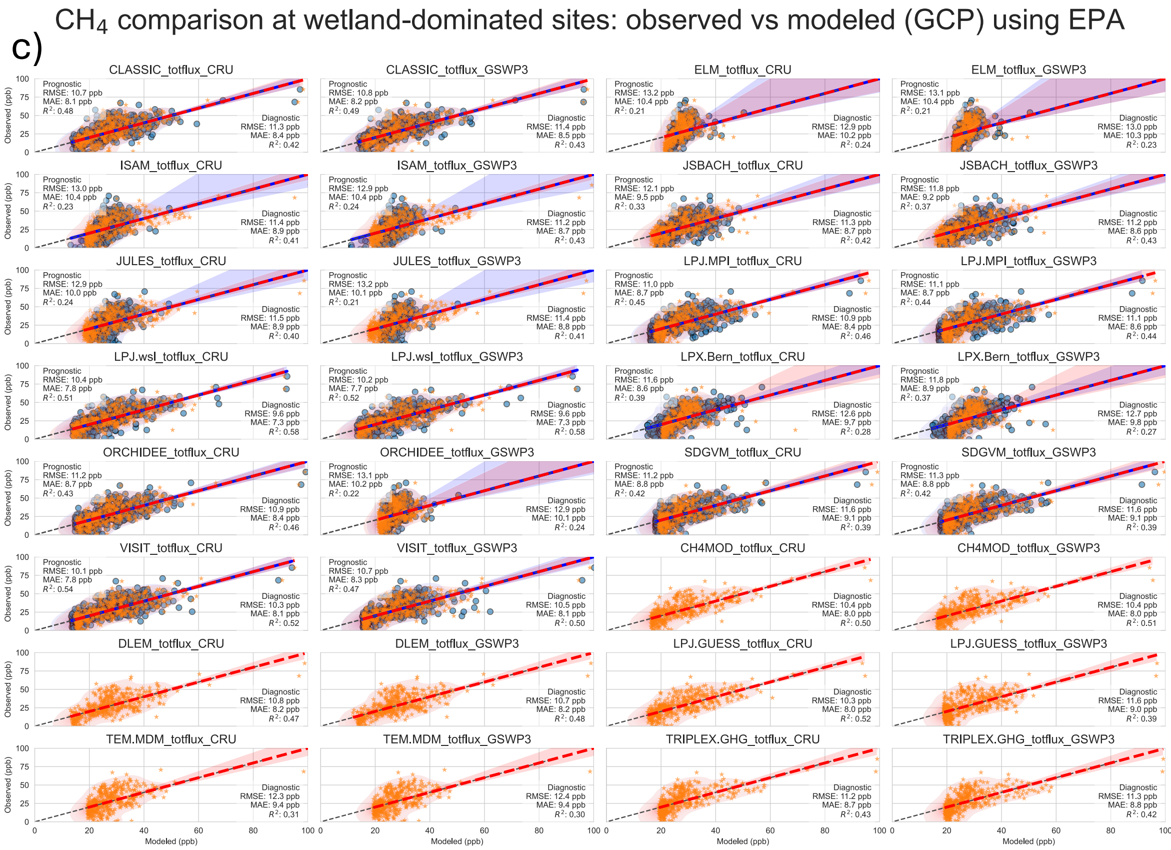

Figure S3. The correlation coefficients and R^2 values between the observed CH_4 increments and the predicted values derived from the GCP models using a multiple linear regression approach. The regression results are shown in panel (a) using CAMS as the anthropogenic flux product. In panel (b), we use the CarbonTracker anthropogenic flux product. And in panel (c), we use the combination of the gridded U.S. EPA CH_4 inventory and Scarpelli's anthropogenic CH_4 flux products covering the regions of Canada and Alaska (Maasakkers et al., 2023; Scarpelli et al., 2021). The blue dots represent the regression results using the prognostic GCP models, and the orange dots represent the regression results using the diagnostic models. The black line in each panel is a 1:1 line, and the colored lines show estimated regression lines. The shaded colors represent the 95% confidence intervals of the regression lines.

Comparisons between GCP models and atmospheric observations by biome

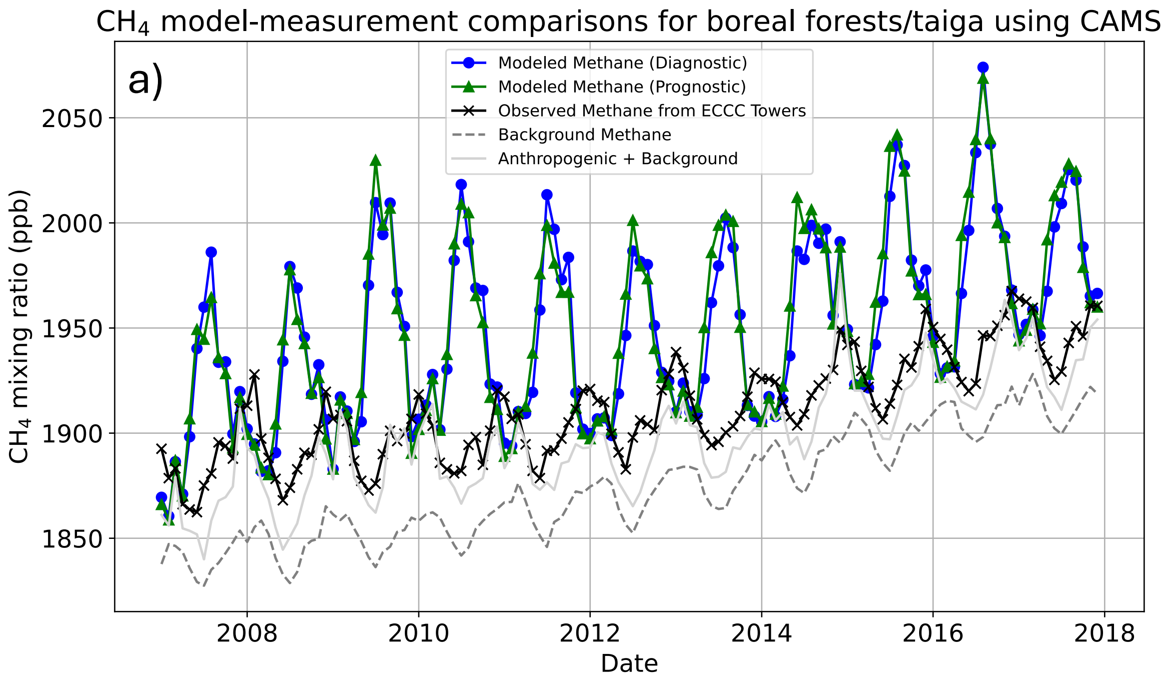

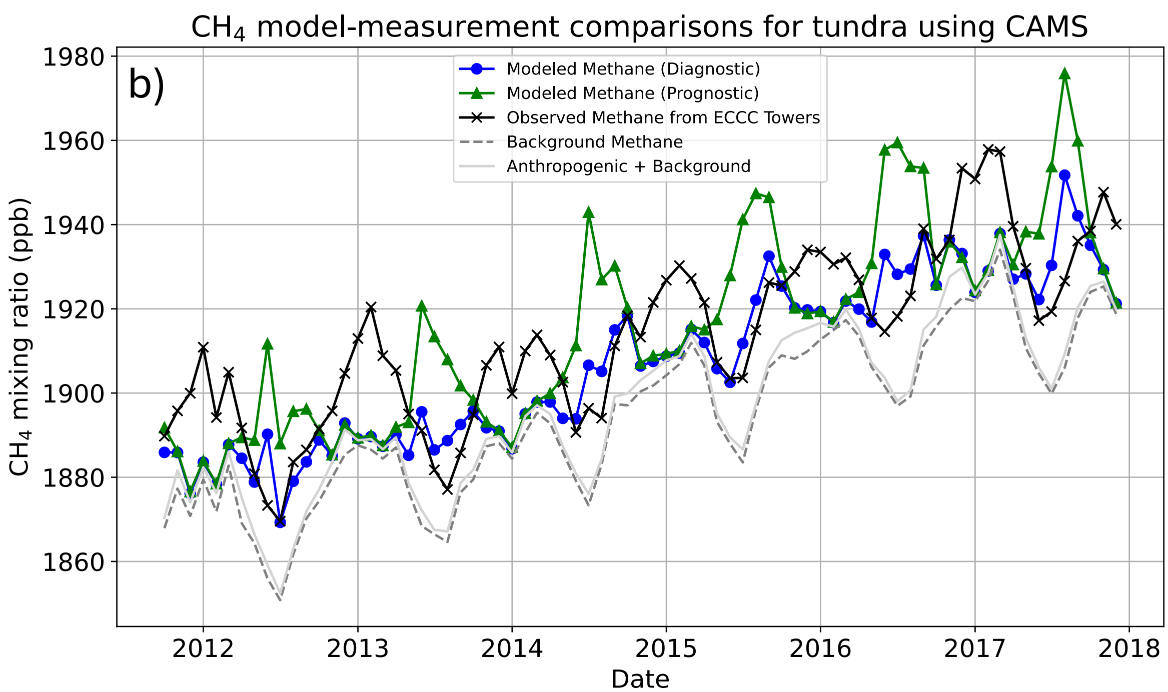

Figure S4. A time series of the mean modeled CH_4 mixing ratios using the STILT model with anthropogenic fluxes from CAMS and wetland fluxes set at the mean of the GCP ensemble across different biomes at ten wetland dominated sites between 2007 and 2017. The two panels correspond to: a) Boreal Forests and Taiga and b) Tundra. The dashed gray line represents the boundary conditions, while the solid gray line shows the sum of the boundary conditions and modeled anthropogenic mixing ratios using CAMS. The green line indicates the total modeled mixing ratios from prognostic models, and the blue line represents those from diagnostic models.

Annual CH_4 flux total using the WETCHIMP models

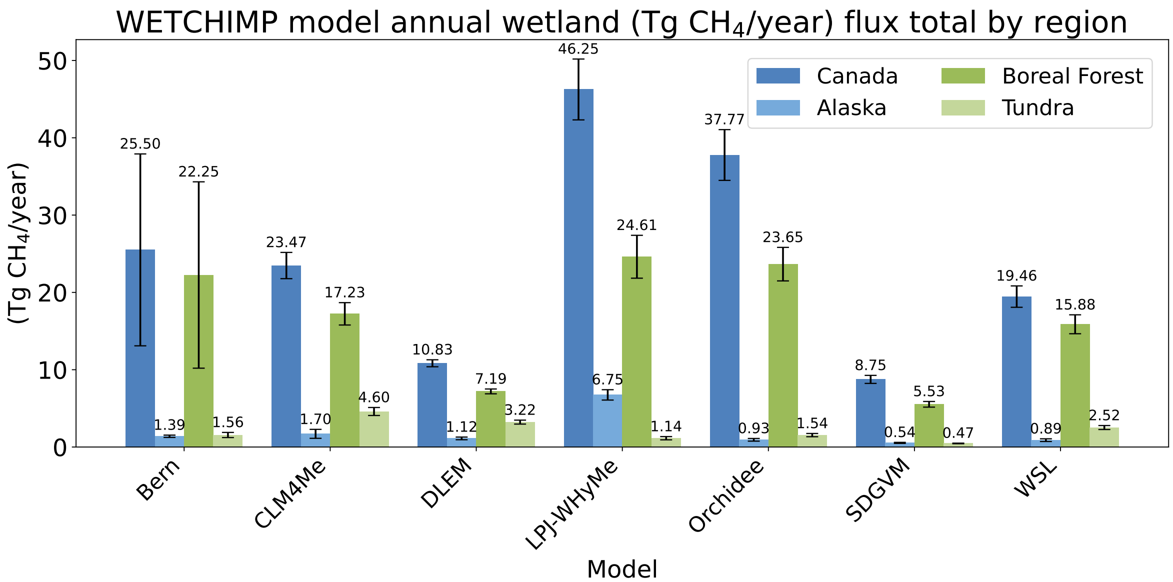

Figure S5. Averaged annual CH_4 flux totals by region and biome type using the WETCHIMP models, averaged across years 1993-2004. There are seven total models included (shown on the x-axis), and the y-axis represents the total annual fluxes in Tg CH_4 per year. The uncertainty bars represent the standard deviations of the annual CH_4 flux totals across different years.

Annual CH_4 flux total using the GCP (diagnostic) models

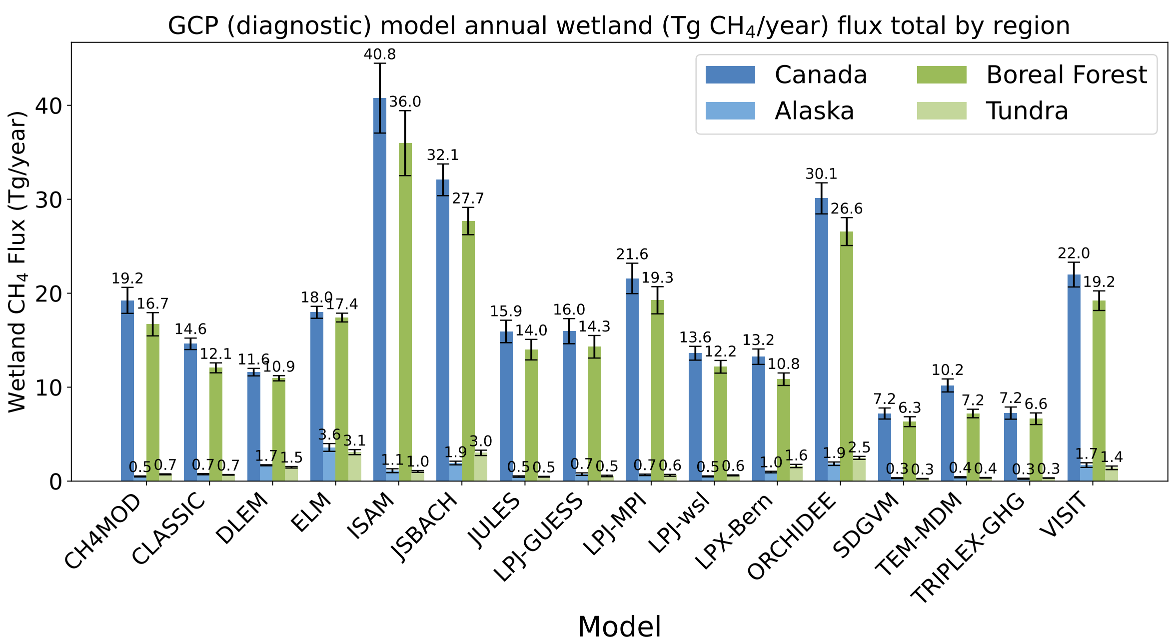

Figure S6. Averaged annual CH_4 flux totals by region and biome type using the GCP models, averaged across years 2007-2017. There are sixteen total models included (shown on the x-axis), and the y-axis represents the total annual fluxes in Tg CH_4 per year. The uncertainty bars represent the standard deviations of the annual CH_4 flux totals across different years.

Mean R^2 and RMSE for the 16 GCP models

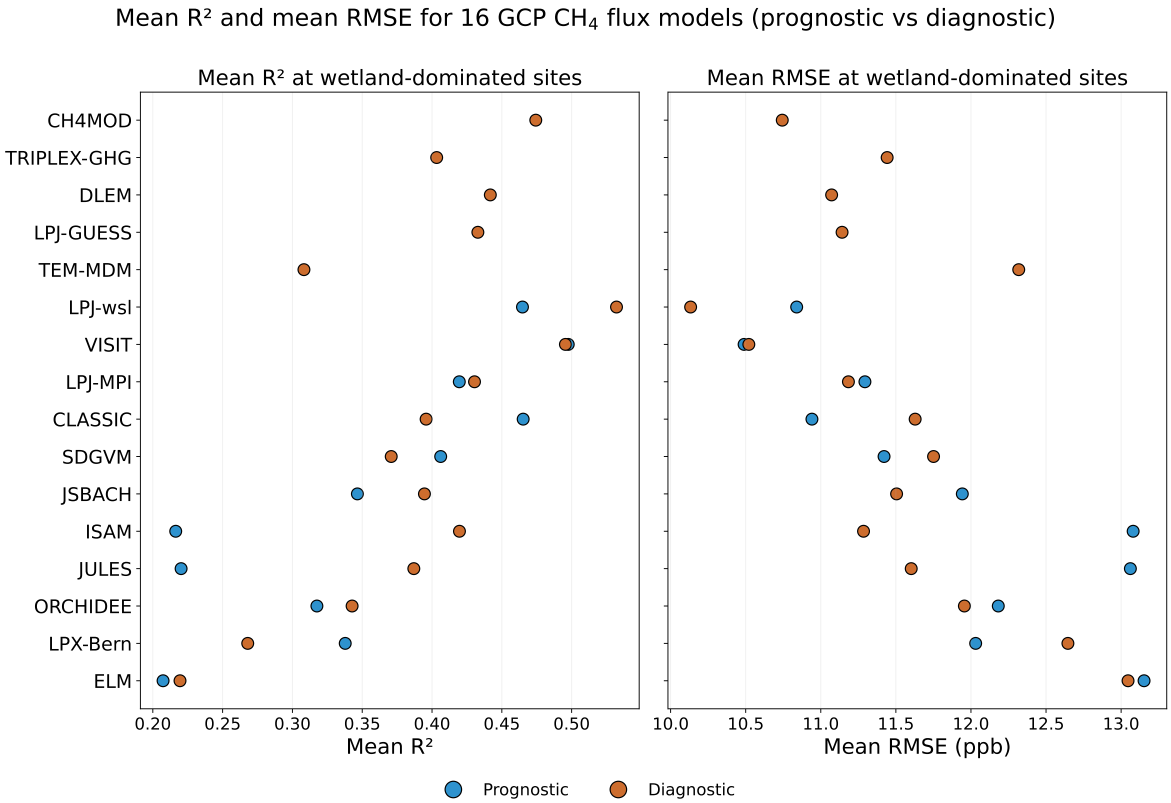

Figure S7. On the left panel, the y-axis lists all the prognostic and diagnostic GCP models, and x-axis shows the R^2 range for these GCP models. And on the right panel, the y-axis lists all the prognostic and diagnostic GCP models, and x-axis shows the RMSE between modeled CH_4 mixing ratios using the GCP models and atmospheric observations. Blue dots represent R^2 and RMSE values for prognostic models across different climate forcing data and anthropogenic products. Orange dots represent R^2 and RMSE values for diagnostic models across different climate forcing data and anthropogenic products.

Seasonal cycle of the anthropogenic fluxes

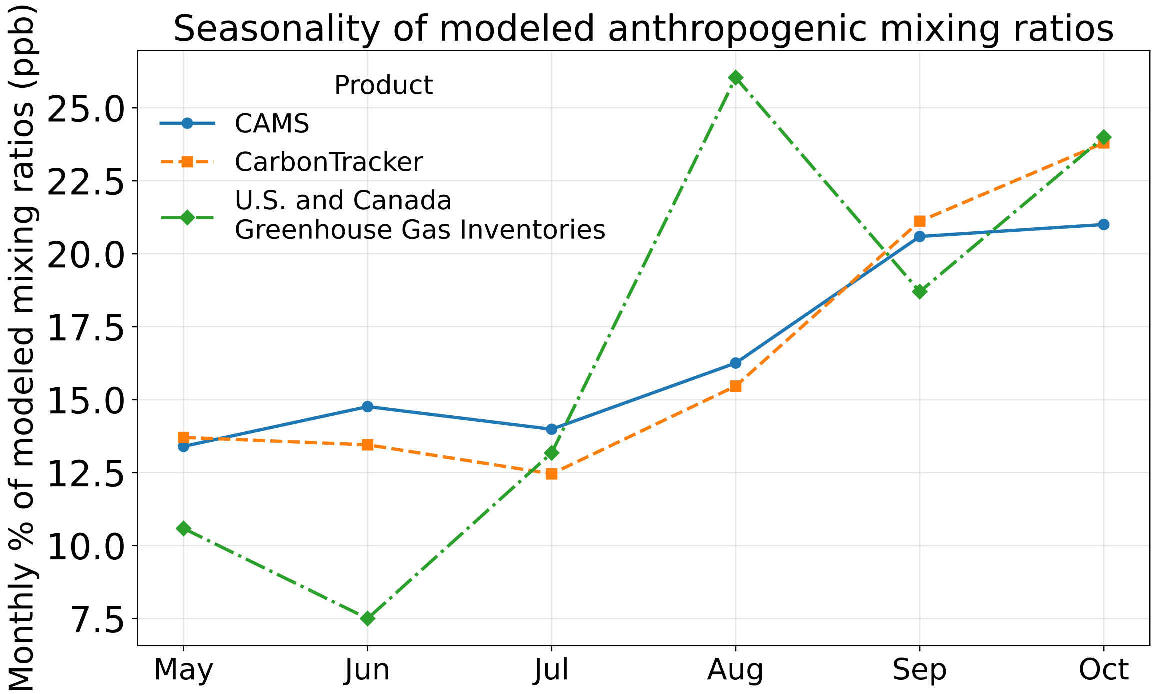

Figure S8. The seasonal cycles of modeled CH_4 mixing ratios using three different anthropogenic flux products from May to October between 2007 and 2017.

Differences in inter-model uncertainty between the shared WETCHIMP and GCP models

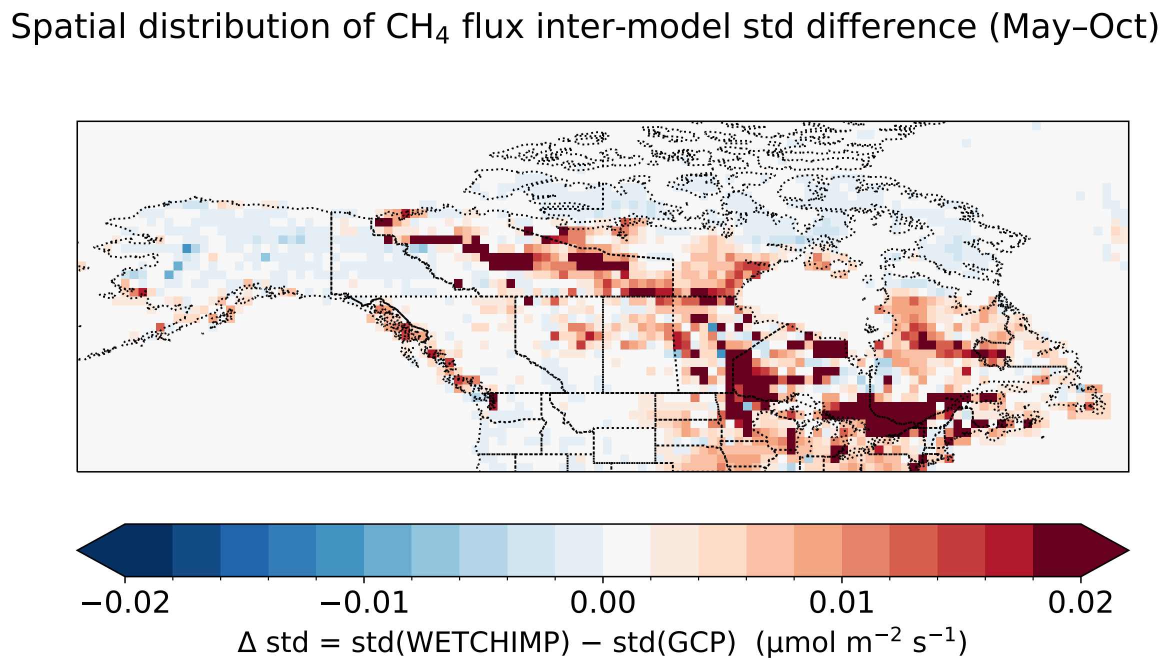

Figure S9. The difference of inter-model standard deviation for each individual model grid box (Fig 3b - Fig 3a), calculated using the 4 overlapping prognostic GCP models and WETCHIMP models (LPX-Bern, SDGVM, ORCHIDEE, LPJ-wsl). Positive values in each grid means that the WETCHIMP models have larger inter-model uncertainty than the GCP models. The inter-model uncertainty in Canada is higher for the WETCHIMP models than the GCP models, but lower for the WETCHIMP models than the GCP models in Alaska. All fluxes have units μmol m^{-2} s^{-1}.

Mean R^2 and RMSE for WETCHIMP and GCP model ensembles

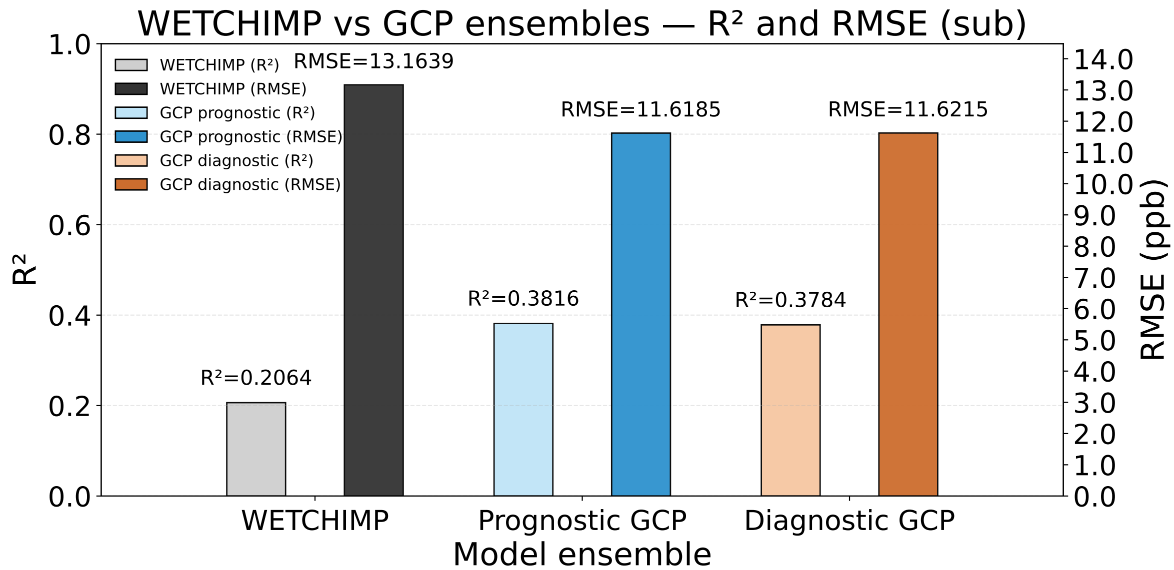

Figure S10. A comparison between the WETCHIMP and GCP model ensembles, including only the models that are common to both ensembles (LPX-Bern, ORCHIDEE, LPJ-wsl, and SDGVM). The left y-axis represents R^2 range for each model ensemble, and the right y-axis represents RMSE range for each model ensemble. The x-axis lists each of the model ensemble: WETCHIMP, prognostic GCP, and diagnostic GCP. The gray and black bars denote WETCHIMP model ensemble, the blue bars denote GCP prognostic ensemble, and the organge bars denote GCP diagnostic ensemble.

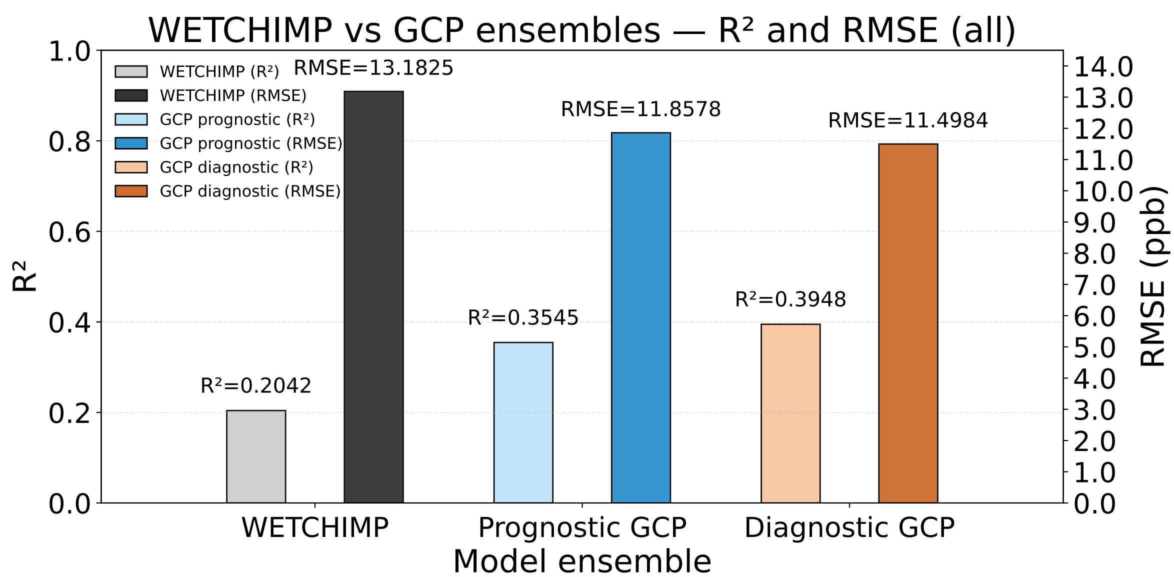

Figure S11. A comparison between the WETCHIMP and GCP model ensembles, including all models. The left y-axis represents R^2 range for each model ensemble, and the right y-axis represents RMSE range for each model ensemble. The x-axis lists each of the model ensemble: WETCHIMP, prognostic GCP, and diagnostic GCP. The gray and black bars denote WETCHIMP model ensemble, the blue bars denote GCP prognostic ensemble, and the organge bars denote GCP diagnostic ensemble.

Analysis of estimated Q_{10} values

We assess the relationship between wetland CH_4 fluxes from the GCP models and temperatures by fitting Q_{10} curves for each GCP model. The Q_{10} factor illustrates how CH_4 wetland fluxes change with a per 10-degree change in temperatures, and a higher Q_{10} means that wetland fluxes are more sensitive to temperature changes (e.g., James, 1953; Mundim et al., 2020; van Hulzen et al., 1999). Several of the GCP models explicitly include a Q_{10} function within the model equations, whereas other models use different functions or modeling schemes to parameterize the relationships between CH_4 fluxes and temperature. Even though not all of the GCP models explicitly use a Q_{10} function, we nevertheless fit each of the flux estimates to a Q_{10} function. Doing so allows us to directly compare the apparent temperature relationships in the different GCP models. Furthermore, to account for the impact of inundation dynamics, we adjust the fluxes by multiplying them by the corresponding inundation fraction at each grid cell. This adjustment normalizes the fluxes to a standard wetland area, demonstrating a more consistent comparison of how wetland CH_4 fluxes respond to temperature variations.

The following formula represents the Q_{10} function (e.g., Mundim et al., 2020; Zhang et al., 2025):

$$R(T) = R_b \cdot Q_{10}^{\frac{(T-T_{\mathrm{ref}})}{10}} \tag{S1}$$

where $R(T)$ are monthly wetland CH_4 fluxes at near-surface air temperature T (°C) based on the same meteorological products used to generate the GCP models, and R_b is the baseline flux at a reference temperature. In this study, we set the reference temperature T_{ref} at 15°C, and the exponential term shows the difference between an ambient temperature and the reference temperature of 15°C, capturing the proportional change in wetland CH_4 flux with temperature. We use the Nelder-Mead method to simultaneously optimize the parameters R_b and Q_{10} by minimizing the sum of squared errors between the predicted fluxes $R(T)$ and the actual wetland CH_4 fluxes from the GCP models (Gao & Han, 2012).

We do not find any correlation between wetland CH_4 fluxes from the GCP models and Q_{10} values, meaning that models with the highest wetland CH_4 fluxes do not always have the highest temperature sensitivity (Fig. S12). ELM has the lowest Q_{10} value of all models at 1.77, suggesting that CH_4 fluxes in ELM are relatively insensitive to temperature changes compared to other models. In contrast, most of the other prognostic and diagnostic GCP models exhibit Q_{10} values greater than 2, with the prognostic ISAM model showing the highest Q_{10} of 11.92, suggesting a stronger temperature dependence.

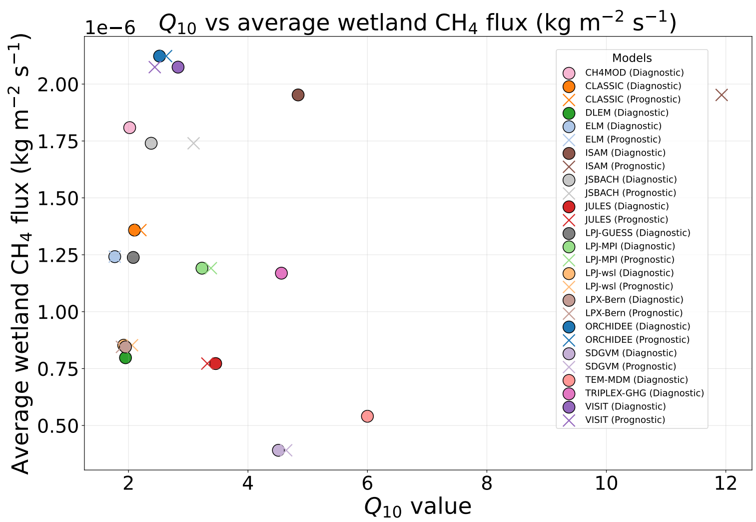

Figure S12. The plot shows the Q_{10} factors estimated for each of the GCP models. Each colored shape represents an unique GCP model, and prognostic and diagnostic values are plotted separately for each model. The plot also shows the relationship between the magnitude of fluxes estimated by each model for the study domain and the Q_{10} value estimated for each model.

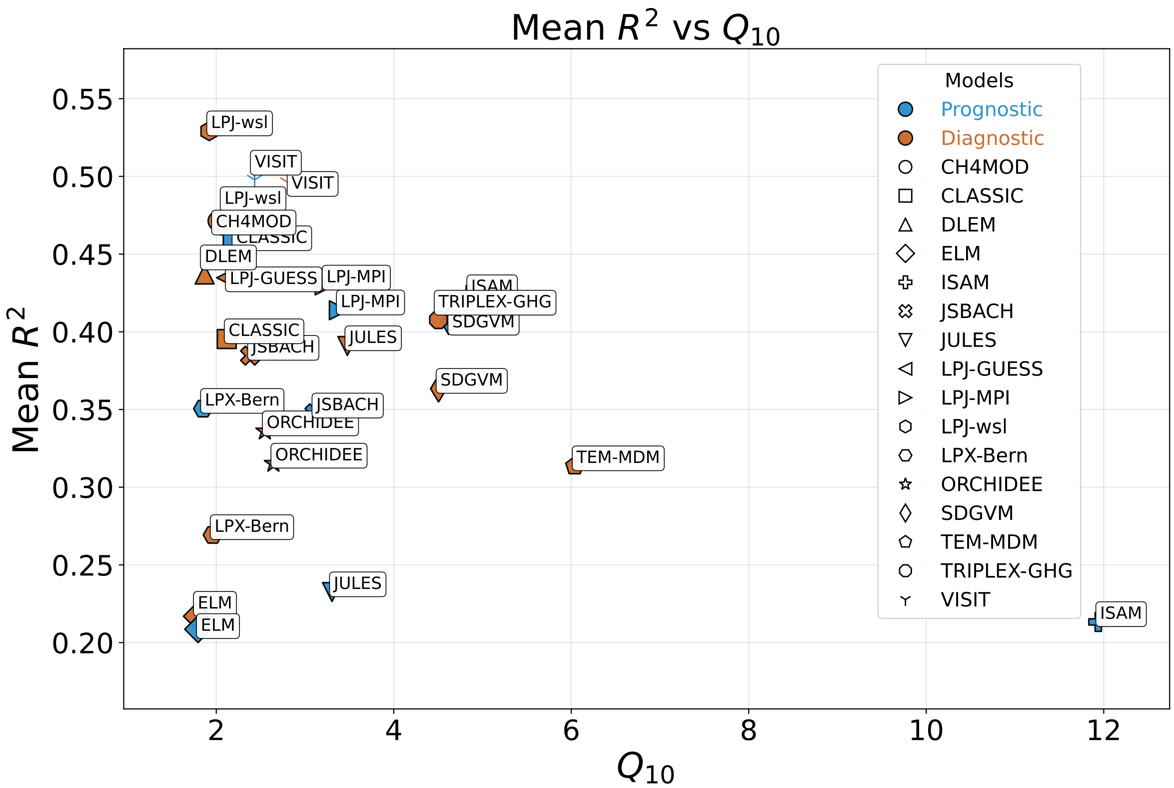

Figure S13. The y-axis represents the mean R^2 values for each GCP model, and the x-axis represents the range of Q_{10} factors estimated for each of the GCP models. Each colored shape represents an unique GCP model, where blue shapes represent prognostic GCP models and orange shapes denote diagnostic GCP models.

References

Arora, V. K., Melton, J. R., & Plummer, D. (2018). An assessment of natural methane fluxes simulated by the CLASS-CTEM model. *Biogeosciences*, *15*(15), 4683–4709. https://doi.org/10.5194/bg-15-4683-2018

Clark, D. B., Mercado, L. M., Sitch, S., Jones, C. D., Gedney, N., Best, M. J., Pryor, M., Rooney, G. G., Essery, R. L. H., Blyth, E., Boucher, O., Harding, R. J., Huntingford, C., & Cox, P. M. (2011). The Joint UK Land Environment Simulator (JULES), model description – Part 2: Carbon fluxes and vegetation dynamics. *Geoscientific Model Development*, *4*(3), 701–722. https://doi.org/10.5194/gmd-4-701-2011

Gao, F., & Han, L. (2012). Implementing the Nelder-Mead simplex algorithm with adaptive parameters. *Computational Optimization and Applications*, *51*, 259–277. https://doi.org/10.1007/s10589-010-9329-3

Ito, A., & Inatomi, M. (2012). Use of a process-based model for assessing the methane budgets of global terrestrial ecosystems and evaluation of uncertainty. *Biogeosciences*, *9*(2), 759–773.

James, W. (1953). *Plant Respiration*. Clarendon Press. https://books.google.com/books?id=9KkvAAAAIAAJ

Kleinen, T., Brovkin, V., & Schuldt, R. J. (2012). A dynamic model of wetland extent and peat accumulation: results for the Holocene. *Biogeosciences*, *9*(1), 235–248. https://doi.org/10.5194/bg-9-235-2012

Kleinen, T., Mikolajewicz, U., & Brovkin, V. (2020). Terrestrial methane emissions from the Last Glacial Maximum to the preindustrial period. *Climate of the Past*, *16*(2), 575–595. https://doi.org/10.5194/cp-16-575-2020

Li, T., Huang, Y., Zhang, W., & Song, C. (2010). CH_4MODwetland: A biogeophysical model for simulating methane emissions from natural wetlands. *Ecological Modelling*, *221*(4), 666–680. https://doi.org/https://doi.org/10.1016/j.ecolmodel.2009.05.017

Liu, L., Zhuang, Q., Oh, Y., Shurpali, N. J., Kim, S., & Poulter, B. (2020). Uncertainty quantification of global net methane emissions from terrestrial ecosystems using a mechanistically based biogeochemistry model [e2019JG005428 2019JG005428]. *Journal of Geophysical Research: Biogeosciences*, *125*(6), e2019JG005428. https://doi.org/https://doi.org/10.1029/2019JG005428

Maasakkers, J. D., McDuffie, E. E., Sulprizio, M. P., Chen, C., Schultz, M., Brunelle, L., Thrush, R., Steller, J., Sherry, C., Jacob, D. J., Jeong, S., Irving, B., & Weitz, M. (2023). A gridded inventory of annual 2012–2018 U.S. anthropogenic methane emissions [PMID: 37857355]. *Environmental Science & Technology*, *57*(43), 16276–16288. https://doi.org/10.1021/acs.est.3c05138

McGuire, A. D., Christensen, T. R., Hayes, D., Heroult, A., Euskirchen, E., Kimball, J. S., Koven, C., Lafleur, P., Miller, P. A., Oechel, W., Peylin, P., Williams, M., & Yi, Y. (2012). An assessment of the carbon balance of arctic tundra: Comparisons among observations, process models, and atmospheric inversions. *Biogeosciences*, *9*(8), 3185–3204. https://doi.org/10.5194/bg-9-3185-2012

Mundim, K. C., Baraldi, S., Machado, H. G., & Vieira, F. M. (2020). Temperature coefficient (Q10) and its applications in biological systems: Beyond the Arrhenius theory. *Ecological Modelling*, *431*, 109127. https://doi.org/https://doi.org/10.1016/j.ecolmodel.2020.109127

Olson, D. M., Dinerstein, E., Wikramanayake, E. D., Burgess, N. D., Powell, G. V. N., Underwood, E. C., D'Amico, J. A., Strand, H. E., Morrison, J. C., Loucks, C. J., Allnutt, T. F., Ricketts, T. H., Kura, Y., Lamoreux, J. F., Wettengel, W. W., Hedao, P., & Kassem, K. (2001). Terrestrial ecoregions of the world: A new map of life on earth. *BioScience*, *51*(11), 933–938.

Ringeval, B., de Noblet-Ducoudré, N., Ciais, P., Bousquet, P., Prigent, C., Papa, F., & Rossow, W. B. (2010). An attempt to quantify the impact of changes in wetland extent on methane emissions on the seasonal and interannual time scales. *Global Biogeochemical Cycles*, *24*(2). https://doi.org/https://doi.org/10.1029/2008GB003354

Scarpelli, T., Jacob, D., Moran, M., Reuland, F., & Gordon, D. (2021). *Gridded inventory of Canada's anthropogenic methane emissions for 2018*. https://doi.org/10.7910/DVN/CC3KLO

Shu, S., Jain, A. K., & Kheshgi, H. S. (2020). Investigating wetland and nonwetland soil methane emissions and sinks across the contiguous United States using a land surface model [e2019GB006251 2019GB006251]. *Global Biogeochemical Cycles*, *34*(7), e2019GB006251. https://doi.org/https://doi.org/10.1029/2019GB006251

Singarayer, J. S., Valdes, P. J., Friedlingstein, P., Nelson, S., & Beerling, D. J. (2011). Late holocene methane rise caused by orbitally controlled increase in tropical sources. *Nature*, *470*(7332), 82–85. https://doi.org/10.1038/nature09739

Spahni, R., Wania, R., Neef, L., van Weele, M., Pison, I., Bousquet, P., Frankenberg, C., Foster, P. N., Joos, F., Prentice, I. C., & van Velthoven, P. (2011). Constraining global methane emissions and uptake by ecosystems. *Biogeosciences*, *8*(6), 1643–1665. https://doi.org/10.5194/bg-8-1643-2011

Tian, H., Xu, X., Liu, M., Ren, W., Zhang, C., Chen, G., & Lu, C. (2010). Spatial and temporal patterns of CH_4 and N_2O fluxes in terrestrial ecosystems of North America during 1979–2008: application of a global biogeochemistry model. *Biogeosciences*, *7*(9), 2673–2694. https://doi.org/10.5194/bg-7-2673-2010

van Hulzen, J., Segers, R., van Bodegom, P., & Leffelaar, P. (1999). Temperature effects on soil methane production: An explanation for observed variability. *Soil Biology and Biochemistry*, *31*(14), 1919–1929. https://doi.org/https://doi.org/10.1016/S0038-0717(99)00109-1

Wania, R., Ross, I., & Prentice, I. C. (2010). Implementation and evaluation of a new methane model within a dynamic global vegetation model: LPJ-WHyMe v1.3.1. *Geoscientific Model Development*, *3*(2), 565–584. https://doi.org/10.5194/gmd-3-565-2010

Zhang, Z., Poulter, B., Melton, J. R., Riley, W. J., Allen, G. H., Beerling, D. J., Bousquet, P., Canadell, J. G., Fluet-Chouinard, E., Ciais, P., Gedney, N., Hopcroft, P. O., Ito, A., Jackson, R. B., Jain, A. K., Jensen, K., Joos, F., Kleinen, T., Knox, S. H., … Zhuang, Q. (2025). Ensemble estimates of global wetland methane emissions over 2000–2020. *Biogeosciences*, *22*(1), 305–321. https://doi.org/10.5194/bg-22-305-2025

Zhang, Z., Zimmermann, N. E., Kaplan, J. O., & Poulter, B. (2016). Modeling spatiotemporal dynamics of global wetlands: comprehensive evaluation of a new sub-grid TOPMODEL parameterization and uncertainties. *Biogeosciences*, *13*(5), 1387–1408. https://doi.org/10.5194/bg-13-1387-2016

Zhu, Q., Liu, J., Peng, C., Chen, H., Fang, X., Jiang, H., Yang, G., Zhu, D., Wang, W., & Zhou, X. (2014). Modelling methane emissions from natural wetlands by development and application of the TRIPLEX-GHG model. *Geoscientific Model Development*, *7*(3), 981–999.

Zhu, Q., Riley, W. J., Tang, J., Collier, N., Hoffman, F. M., Yang, X., & Bisht, G. (2019). Representing nitrogen, phosphorus, and carbon interactions in the E3SM land model: Development and global benchmarking. *Journal of Advances in Modeling Earth Systems*, *11*(7), 2238–2258. https://doi.org/https://doi.org/10.1029/2018MS001571